NUMERICAL SIMULATION OF ROTOR AERODYNAMICS USING QUASI-1D SCHEMES ON UNSTRUCTURED MESHES

I. V. Abalakin, V. G. Bobkov, T. K. Kozubskaya
Keldysh Institute of Applied Mathematics, Miusskaya pl. 4, Moscow, 125047 Russia
V. A. Anikin
Design office "Kamov", ul. 8 Marta 8-A, Lyubertsy, Moscow oblast, 111625 Russia

OVERVIEW

The paper is devoted to the numerical simulation of aerodynamic characteristics of helicopter rotors in hover using higher-accuracy lower-cost algorithm on unstructured meshes.

The helicopter rotor construction is being constantly developed and inevitably complicated. It is connected with the permanent necessity to optimize the shapes in order to improve aerodynamic characteristics of rotors. In this situation mathematical modeling and numerical simulation become one of the efficient tools since it offers a possibility to easily change the rotor geometry and flight regimes and to perform serial predictions needed for the optimization and production.

The rotor geometry is primarily determined by the blades. The blade shapes are composed of basic varying elements such as tips, twists and constitutive airfoils. To handle complicated changeable geometry of a blade numerically, an efficient way is to use unstructured meshes. To carry out the corresponding computations for reasonable time, high accuracy numerical schemes and efficient parallel algorithms for multi-CPU computer systems are needed.

In the talk we present a numerical technique for predicting rotor aerodynamics. The numerical algorithm is generally applicable to all the family of models based on the Euler equations within DNS, RANS, LES and hybrid RANS-LES approaches for simulating compressible turbulent flows. However in the predictions considered here we use the Euler and Navier-Stokes equations taken in non-inertial reference framework.

A feature of the numerical technique presented is the usage of vertex-centered EBR scheme, [1], [2]) for unstructured meshes which provides accuracy higher than most second order schemes in terms of error values and takes lower computational costs in comparison with very high order algorithms. The higher accuracy of the scheme is provided due to the quasi-1D edge-based reconstruction of variables involved in the calculation of fluxes arbitrary unstructured meshes. As a result, when operating on uniform grid-like meshes the scheme possess the accuracy of the 5^{th} order. For the time advancing we use the second order implicit scheme with BiGSStab method for solving linear algebraic equations. The numerical techniques are implemented in the in-house code NOISEtte++ [3] for solving aerodynamics and aeroacoustics problems on unstructured meshes. The hybrid MPI-OpenMP parallel model of NOISEtte++ allows its efficient performance on tens thousands of CPU-cores.

We demonstrate an efficiency of the numerical tools on solving two model problems on rotor aerodynamics in hover.

The first problem considers the configuration "rotor in a ring". The rotor installed in toroidal channel ("ring") consists of four blades located in the same disc plane and a central body. The blades are based on one airfoil with the liner twist. We consider the case of the same pitch angle for all the blades.

In the second problem we simulate the flow generated by the model main rotor. The rotor consists of four blades of complicated configuration based on five different airfoils. The blade geometry includes piecewise linear twist and swept tip.

The study was carried out within the framework of the Program of Applied Scientific Investigations "Development of the Software for Modeling Aerodynamic and Aeroacoustic Characteristics of Helicopter Rotors on Supercomputers" (unique identifier of the project RFMEFI160414X0092) of the Federal Goal-Oriented Program "Investigations and Developments in the Top Priority Lines of the Development of the Science and Engineering Complex of Russia for the Years 2014–2020" of the Ministry of Education and Science of the Russian Federation in the Top Priority Line "Transport and Space Systems".

1. PROBLEM OF VISCOUS FLOW AROUND ROTOR

1.1. Shrouded rotor case

The geometry of the model under consideration is based on an actual experimental setup representing a shrouded four-blade tail rotor. In the channel there is a single rotor without details of its mechanization, while the channel (ring), where the rotor rotates, represents an axisymmetric body of revolution. The central body is in the shape of a cylinder with rounded end faces.

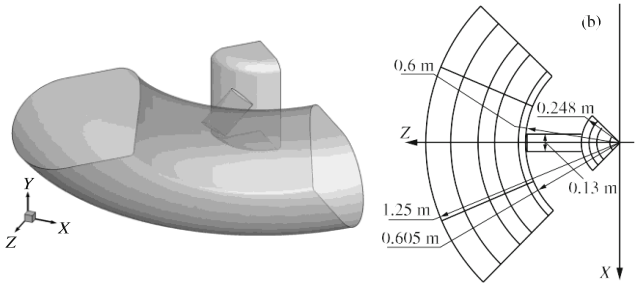

Fig. 2. Shrouded rotor sector with one blade; geometry (left) and dimensions (right).

As mentioned above, due to the symmetry of this formulation in the absence of external flow the problem is solved for a sector with the angle $2\pi/N$ (N = 4) containing one rotor blade (Figs. 1b and 2a), the periodic boundary conditions being imposed on the lateral planes of the sector in the azimuthal direction.

In accordance with the description of the experimental setup, the radius of the central body, to which the blade is fastened, is taken to be 0.248 m, the rotor radius being R = 0.6 m. The blade chord b = 0.13 m. The blade surface is based on the TsAGI SV-11 airfoil with the linear twist $\varphi_{sw}(r) = 40\left(0.7 - r/R\right)/3$, where r is the distance to the axis of rotation of the rotor. The outside channel radius is 1.25 m, while the inside channel radius in the plane of rotation of the rotor is 0.605 m, which corresponds to a 5 mm gap between the blade end and the inside surface of the channel (Fig. 2b). We consider the rotor rotation regime at a frequency of 19.44 Hz, which corresponds to the angular velocity ω = 122.17 rad/s and the linear velocity of the blade end $V_{blade} = \omega R$ = 73.3 m/s; the angle of pitch of the blade φ can take the values of 10°, 15°, 20°, 30°, and 40°. The Reynolds number is determined as $\mathrm{Re} = \rho_0 V_{blade}\, b/\mu_0$ and takes the value $\mathrm{Re} = 6.28 \times 10^5$ for the values ρ_0 = 1.2041 kg/m^3 and $\mu_0 = 1.827 \times 10^{-5}$ N·s/m^2 corresponding to the air density and dynamic viscosity at the temperature of 20° C.

1.2. Main rotor case

The geometry of the second case is also based on an actual experimental setup representing model main rotor. The blade of the four-blade rotor surface based on the set of TsAGI airfiols with linear twist and the swept tip. The rotor radius is R = 1.952 m and the blade chord b = 0.18 m (Fig. 3).

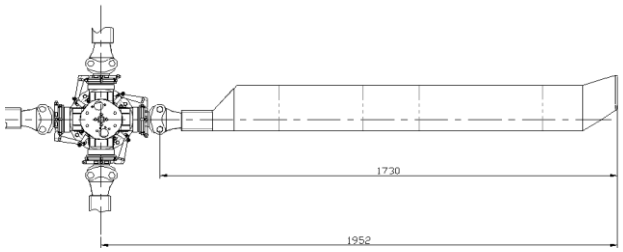

Fig. 3. Main rotor blade.

We consider the rotor rotation regime at a frequency of 11.14 Hz (668.4 RPM), which corresponds to the angular velocity ω = 70 rad/s and the linear velocity of the blade end $V_{blade} = \omega R$ = 136.63 m/s; the angle of pitch of the blade φ can take the values of 5°, 10°, 15° and 20°. The Reynolds number is determined as $\mathrm{Re} = \rho_0 V_{blade}\, b/\mu_0$ and takes the value $\mathrm{Re} = 1.6 \times 10^6$ for the values ρ_0 = 1.2041 kg/m^3 and $\mu_0 = 1.827 \times 10^{-5}$ N·s/m^2 corresponding to the air density and dynamic viscosity at the temperature of 17° C.

2. THE PROBLEM CHARACTERISTICS UNDER STUDY

2.1. Aerodynamic forces of the rotor

In the problems of the type described above the main parameters characterizing the properties of the configuration under study are the coefficients of aerodynamic forces, namely, the thrust and torque coefficients.

We will determine the aerodynamic forces of the blade and the segment of the surrounding ring following the book [4]. For this purpose, we will consider two reference frames (Fig. 4), namely, the fixed coordinate system (x, y, z) and a coordinate system (x', y', z') fitted to the rotatable blade and obtained by rotation of the fixed coordinate system by an angle $\psi(t) + \pi/2$, where the angle $\psi(t)$ is determined by the angular velocity of blade rotation: $\psi(t) = \omega t$.

Since the calculations are made in the rotatable coordinate system, including the case of stationary solution (the dependence on the azimuthal angle ψ is absent), the axes of the fixed and rotatable coordinate systems can be identified.

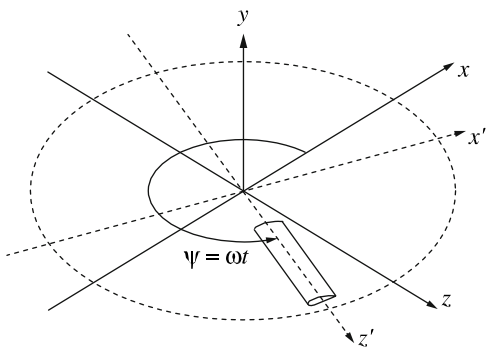

Fig. 4. Fixed and rotatable coordinate systems.

Let $p(x,y,z)$ be the pressure distribution over the blade surface *S* and n_x, n_y, and n_z be the components of the unit normal outward with respect to the surface *S*. Then the *N*-bladed rotor thrust T_{rot} is composed of the forces T_y^{blade} normal to the plane of rotation and acting on single blades

(2.1) $$T^{rot} = NT_y^{blade} = N\int_S pn_y\, ds.$$

The rotor force moment is determined by the force projections on the axes of the fixed coordinate system and the radius-vector (lever) of the blade coordinates in the rotatable coordinate system $\mathbf{r} = (0,0,z) = (0,0,z')$

$$\mathbf{M} = N\int_S p(\mathbf{r}\times\mathbf{n})\, ds.$$

Hence there follows the expression for the aerodynamic torque of the rotor

$$M_k^{rot} = M_y = N\int_S zpn_x\, ds.$$

In the case of the stationary solution the averaging over the azimuthal angle is not made in the above expressions for the thrust and the torque.

Let now $p(x,y,z)$ be the pressure distribution over the surface of a ring sector with the angle of $2\pi/N$. This pressure distribution corresponds to the fixed blade position near the ring at a certain moment of time (the pressure distribution in the rotatable coordinate system). For this reason, to determine the pressure distribution in the fixed coordinate system requires averaging the pressure over the azimuthal angle ψ.

In the case of steady flow the angle-average pressure is the same for any of *N* segments. Then, passing to the cylindrical coordinates (r,ψ,z) we can calculate the azimuthal-angle-average pressure

$$\langle p\rangle(r,z) = \int_0^{2\pi} p(r,\psi,z)\, d\psi.$$

The ring thrust is calculated from the formula analogous to (2.1)

$$T^{ring} = N\int_S \langle p\rangle n_y\, ds,$$

where *S* is the ring surface and n_x, n_y, and n_z are the components of the unit normal outward with respect to the ring surface. The ring torque is determined by the force projections on the axes of the fixed coordinate system and the radius-vector of the ring coordinates in the fixed coordinate system $\mathbf{r} = (x,y,z)$

$$M_k^{ring} = N\int_S \langle p\rangle(zn_x - xn_z)\, ds.$$

The thrust coefficient c_T and the aerodynamic torque coefficient m_k are determined by nondimensionalizing the thrust and torque values by the quantities $\rho_0 A(\omega R)^2/2$ and $\rho_0 RA(\omega R)^2/2$, respectively

$$c_T^{rot/ring} = \frac{2T^{rot/ring}}{\rho_0 A(\omega R)^2},\quad m_k^{rot/ring} = \frac{2M_k^{rot/ring}}{\rho_0 RA(\omega R)^2},$$

where ρ_0 is the undisturbed flow density, $A = \pi R^2$ is the blade disk area, *R* is the blade radius, and ω is the absolute value of the angular velocity of the blade.

The values of the calculated force coefficients are compared with those obtained in the full-scale experiments.

3. MATHEMATICAL MODEL

3.1. Navier–Stokes equations in a noninertial coordinate system

Flow around the rotatable shrouded blade is calculated from the system of Navier–Stokes equations for a compressible gas written in the noninertial rotatable coordinate system in which the blade in a gas flow is fixed, while the shroud (ring) rotates.

We will denote the absolute velocity vector in the original fixed coordinate system by **u** and introduce a movable coordinate system rotating at a constant angular velocity $\boldsymbol{\omega} = (\omega_x, \omega_y, \omega_z)^T$ about an axis fixed in the original coordinate system.

We will define the relative velocity vector as follows:

$$\mathbf{u}' = \mathbf{u} - \mathbf{V},\ \mathbf{V} = \boldsymbol{\omega}\times\mathbf{r}.$$

We will point out two important properties of the vector of the linear velocity of rotation.

1) The vector **V** gradient, that is, the dyadic product

of the vector operator ∇ and the vector **V** is the skew-symmetric tensor

$$\nabla\mathbf{V} = \nabla \otimes \mathbf{V} = \begin{pmatrix} 0 & -\omega_z & \omega_y \\ \omega_z & 0 & -\omega_x \\ -\omega_y & \omega_x & 0 \end{pmatrix}.$$

From this expression it follows that

$$\text{(3.1)} \qquad \operatorname{div}\mathbf{V} = 0,\ \boldsymbol{\omega} = \frac{1}{2}\operatorname{curl}\mathbf{V},$$

while its symmetric part is zero

$$\text{(3.2)} \qquad \frac{1}{2}\left(\frac{\partial V_i}{\partial x_j} + \frac{\partial V_j}{\partial x_i}\right) = 0.$$

2) It can easily be seen that the vector **V** satisfies the following differential relations

$$\text{(3.3)} \quad (\mathbf{V}\cdot\nabla)\mathbf{V} = \boldsymbol{\omega}\times\mathbf{V} = \boldsymbol{\omega}\times(\boldsymbol{\omega}\times\mathbf{r}), (\mathbf{u}'\cdot\nabla)\mathbf{V} = \boldsymbol{\omega}\times\mathbf{u}'.$$

The system of Navier–Stokes equations written in the rotatable coordinate system in the form of conservation laws with respect to the velocity $\mathbf{u}'$ is as follows (see, for example, [5]):

$$\text{(3.4)} \quad \begin{cases} \dfrac{\partial\rho}{\partial t} + \operatorname{div}\rho\mathbf{u}' = 0, \\ \dfrac{\partial\rho\mathbf{u}'}{\partial t} + \operatorname{div}\rho\mathbf{u}'\otimes\mathbf{u}' + \nabla p = \operatorname{div}\mathbf{S} + \rho\boldsymbol{\omega}\times(\boldsymbol{\omega}\times\mathbf{r}) - 2\rho(\boldsymbol{\omega}\times\mathbf{u}'), \\ \dfrac{\partial E}{\partial t} + \operatorname{div}(E+p)\mathbf{u}' = \operatorname{div}\mathbf{q} + \operatorname{div}\mathbf{S}\mathbf{u}', \end{cases}$$

where $E = \rho\mathbf{u}'^2/2 + \rho\varepsilon$ is the total energy and ε is the internal energy of the gas. System (3.4) is closed by the equation of state for the perfect gas $p = (\gamma-1)\rho\varepsilon$. In system (3.4) **S** is the strain rate tensor defined as

$$\text{(3.5)} \qquad S_{ij} = 2\mu\left(\frac{\partial u_i'}{\partial x_j} + \frac{\partial u_j'}{\partial x_i}\right) - \frac{2}{3}\delta_{ij}\frac{\partial u_i'}{\partial x_i}$$

and the vector **q** is the total energy flux[1]

$$q_i = \frac{\mu}{\gamma\,\mathrm{Pr}}\frac{\partial\varepsilon}{\partial x_i}$$

where the Prandtl number is given by the relation $\mathrm{Pr} = \mu c_p/\lambda$, μ is dynamic viscosity of the gas, c_p is the specific heat at constant pressure, λ is thermal conductivity, and γ is the adiabatic exponent.

Applying Eqs. (3.3) we will bring the system of equations (3.4) into the form using the absolute velocity vector **u**. We note that, in view of Eqs. (3.1) and (3.2), the strain rate tensor (3.3) is invariant with respect to the rotation velocity of the coordinate system and, therefore, replacing the relative velocity by the absolute velocity does not change the strain rate tensor form given by Eq. (3.5).

Finally, the system of Navier–Stokes equations written in the rotatable coordinate system with respect to the absolute velocity vector reads as follows:

$$\text{(3.6)} \quad \begin{cases} \dfrac{\partial\rho}{\partial t} + \operatorname{div}\rho(\mathbf{u}-\mathbf{V}) = 0, \\ \dfrac{\partial\rho\mathbf{u}'}{\partial t} + \operatorname{div}\rho(\mathbf{u}-\mathbf{V})\otimes\mathbf{u} + \nabla p = \operatorname{div}\mathbf{S} - \rho(\boldsymbol{\omega}\times\mathbf{u}), \\ \dfrac{\partial E}{\partial t} + \operatorname{div}E(\mathbf{u}-\mathbf{V}) + \operatorname{div}p\mathbf{u} = \operatorname{div}\mathbf{q} + \operatorname{div}\mathbf{S}\mathbf{u}'. \end{cases}$$

From the standpoint of an observer in the fixed coordinate system the system of equations (3.6) describes the variation in the conservative variables at the expense of their translation in the medium rotating at the velocity **V**, the pressure gradient, and the velocity vector rotation by an angle equal to $|\omega|t$. In numerically realizing this system of equations the rotation velocity may be interpreted as the movable grid velocity. In this form, the system of equations was considered, for example, in [6], [7], where the calculations were simultaneously conducted in both rotatable and fixed domains.

We will rewrite system (3.6) in the pseudovector flux form:

$$\text{(3.7)} \quad \begin{cases} \dfrac{\partial\mathbf{Q}}{\partial t} + \dfrac{\partial\mathbf{F}_x^I}{\partial x} + \dfrac{\partial\mathbf{F}_y^I}{\partial y} + \dfrac{\partial\mathbf{F}_z^I}{\partial z} - \dfrac{\partial\mathbf{F}_x^{NI}}{\partial x} - \dfrac{\partial\mathbf{F}_y^{NI}}{\partial y} - \dfrac{\partial\mathbf{F}_z^{NI}}{\partial z} = \mathbf{H} + \dfrac{\partial\mathbf{F}_x^V}{\partial x} + \dfrac{\partial\mathbf{F}_y^V}{\partial y} + \dfrac{\partial\mathbf{F}_z^V}{\partial z}, \\ \mathbf{Q} = (\rho,\ \rho u,\ \rho v,\ \rho w,\ E)^T, \\ \mathbf{H} = (0, -v\omega_z + w\omega_y,\ u\omega_z - w\omega_x,\ -u\omega_y + v\omega_x,\ 0)^T \end{cases}$$

where $\mathbf{F}_x^I$, $\mathbf{F}_y^I$, and $\mathbf{F}_z^I$, are the convective fluxes of the system of Navier–Stokes equations in the inertial (fixed) coordinate system, $\mathbf{F}_x^{NI} = V_x\mathbf{Q}$, $\mathbf{F}_y^{NI} = V_y\mathbf{Q}$, and $\mathbf{F}_z^{NI} = V_z\mathbf{Q}$ are the additions to the fluxes determined by the noninertial coordinate system or the grid motion velocity, and $\mathbf{F}_x^V$, $\mathbf{F}_y^V$, and $\mathbf{F}_z^V$, are the viscous fluxes of the system of Navier–Stokes equations determined by the gradients of the absolute velocity vector and the heat flux.

The Jacobi matrices of the convective flux initiated by the rotation velocity have the diagonal form:

$$\partial\mathbf{F}_{x,y,z}^V/\partial\mathbf{Q} = V_{x,y,z}\,\mathbf{I}.$$

Therefore, the Jacobi matrices of the total convective flux can be written in the form:

[1] We consider a polytropic gas, which means that the specific heat c_V is temperature- independent and, therefore, the internal energy is the linear function of the temperature: $\varepsilon = c_V T$

$$\frac{\partial\left(\mathbf{F}^{I}_{x,y,z}-\mathbf{F}^{NI}_{x,y,z}\right)}{\partial\mathbf{Q}}=\mathbf{S}_{x,y,z}\,\mathrm{diag}\left(\lambda^{i}_{x,y,z}-V_{x,y,z}\right)\mathbf{S}^{-1}_{x,y,z},\qquad i=1,\ldots,5$$

are the eigenvalues $\lambda^{i}_{x,y,z}$ and $\mathbf{S}_{x,y,z}(\mathbf{S}^{-1}_{x,y,z})$ are the matrices of the right (left) eigenvectors of the Jacobi matrices $\partial\left(\mathbf{F}^{I}_{x,y,z}-\mathbf{F}^{NI}_{x,y,z}\right)\big/\partial\mathbf{Q}$ of the corresponding convective fluxes of the Navier–Stokes equations in the inertial coordinate system. Thus, the difference of system (3.7) from that of Navier–Stokes equations written in the fixed coordinate system is only in the variation in the characteristic velocities and the presence of the source term on the right side. For this reason, in numerically realizing system (3.7) by means of the Godunov-type schemes the approximation methods remain the same as in solving the equations in the fixed coordinate system.

3.2. Boundary conditions

For the system of Navier–Stokes equations the boundary no-slip conditions are imposed on solid boundaries. These consist in equating the relative velocities (in the rotating noninertial coordinate system) at the boundaries to zero. In the case of employing the system of equations (3.6) written with respect to the absolute velocity vector (in the fixed coordinate system) the no-slip conditions are written as follows:

$$\mathbf{u}-\mathbf{V}=0$$

for the rotating blade, where **V** is the linear velocity of the surface rotation, and

$$\mathbf{u}=0$$

for the fixed shroud (ring).

Since the numerical simulation of the problem is performed in a bounded region, some artificial boundary conditions must be imposed on the computation domain boundary.

These boundary conditions are determined by splitting the fluxes relating the values of the gasdynamic parameters ρ_i, $\mathbf{U}_i$, and p_i within the computation domain and their values in the distant flow ρ_∞, $\mathbf{U}_\infty$, and p_∞ in the directions of the characteristic velocities. The latter values are determined by the characteristic relations for an isentropic gas

$$\rho_\infty=\rho_i\left(\frac{p_\infty}{p_i}\right)^{1/\gamma},\quad p_\infty=p_0$$

$$\mathbf{U}_\infty=\mathbf{U}_i+\frac{2}{\gamma-1}\left[\left(\gamma\frac{p_i}{\rho_i}\right)^{1/2}-\left(\gamma\frac{p_\infty}{\rho_\infty}\right)^{1/2}\right]\cdot\mathbf{n},$$

where p_0 is the constant pressure of the undisturbed gas and **n** is the vector of the unit outward normal to the computation domain boundary.

4. NUMERICAL METHOD

4.1. Numerical method for calculating the near flowfield

The method of calculating the near flowfield is based on the solution of the system of Navier–Stokes equations in the noninertial coordinate system (3.7). The spatial approximation of the convective fluxes of this system on tetrahedral grids is realized using a scheme based on the quasi-one-dimensional reconstruction of the variables along a grid edge (EBR scheme). This class of schemes is described in detail in [1], [2], [8]. We note that the spatial discretization is based on the vertex-centered formulation, which means that all the unknown variables are determined at gridpoints surrounded by computation cells (dual grid).

On the tetrahedral grids, for which the dual grid has computation cells of the same shape (analogue of the uniform Cartesian grid), the scheme based on the quasi-one-dimensional reconstruction along a grid edge can be of as high as fifth and even sixth order in space at the corresponding reconstruction of the flux variables [2], [8]. In the case of an arbitrary unstructured tetrahedral grid and the same reconstruction the approximation order is formally only second. However, this scheme ensures a higher accuracy (from the standpoint of the difference between the numerical and exact solutions with respect to the grid norm) than the other second-order schemes [2].

The spatial approximation of the viscous terms in the system of Navier–Stokes equations is realized using the finite-element Galerkin method with linear basis functions.

The time integration is performed using an implicit three-layer second-order scheme followed by the Newtonian linearization of the finite-difference (in space) system of equations. At each Newtonian iteration stage the method of biconjugate gradients (BiCGSTAB) [9] is applied for solving the system of linear equations. The method is realized in the NOISEtte software package [3].

4.2. Computation grid

As mentioned in Sect. 1, the computation domain of the problem is a sector containing one blade. The outer boundary of the computation domain is so

constructed that it describes the flow region produced by the rotor both directly beneath it (along the axis of rotation) and where it is formed above the rotor. The computation domain dimensions outside the ring are so chosen that it is possible to analyze the flow parameters outside the ring and to construct a control surface whose size would be sufficient to analyze the acoustic properties of the shrouded rotor (Fig. 5a).

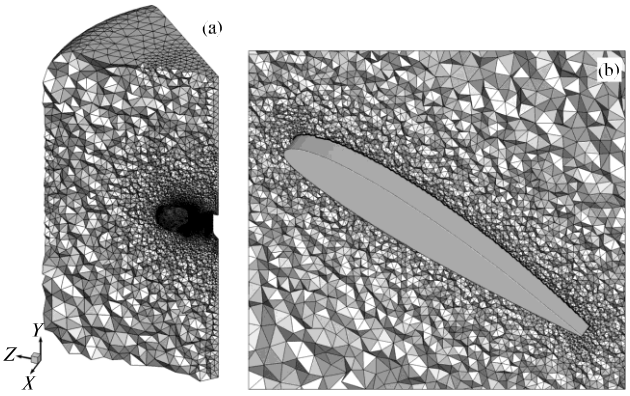

Fig. 5. General view of the computation grid for shrouded rotor; longitudinal section (a) and grid near the blade (b).

An unstructured tetrahedral grid is constructed in the computation domain. It is refined in the regions, where the detailed modeling of the aerodynamic effects is required. Thus, the most detailed grid is constructed on the leading and trailing (along the airfoil chord) regions of the blade surface and on the blade tip. On the surfaces of the blade, the central body, and the ring the grid is refined in the normal-to-surface directions in order to resolve the boundary layer.

Computation grid dimensions for different pitch angles for the shrouded rotor case

Pitch angle α,deg	Mesh nodes number	Number of elements
10	2326941	13589791
15	2371707	13859009
20	2511582	14669900
30	2555652	14936402
40	2592469	15154418

Then the surface and volume grids are constructed using the advancing front technique, so that the grid element dimensions vary smoothly (Fig. 5). The most detailed grid is constructed in the gap region between the blade endface and the inside surface of the ring. Constraints from above on maximum dimensions of the elements near the blade and the central body are also introduced.

On the solid surfaces of the rotor, the central body, and the ring the grid is refined in order to resolve the boundary layer, in accordance with the Reynolds number so that not less than ten cells fall on the boundary layer thickness.

As a result, five computation grids for the blade pitch angles of 10, 15, 20, 30, and 40^o were constructed; their dimensions are given in table.

For the main rotor case four meshes were constructed for each blade pitch angle. The mesh structure was similar to the first case (Fig. 6).

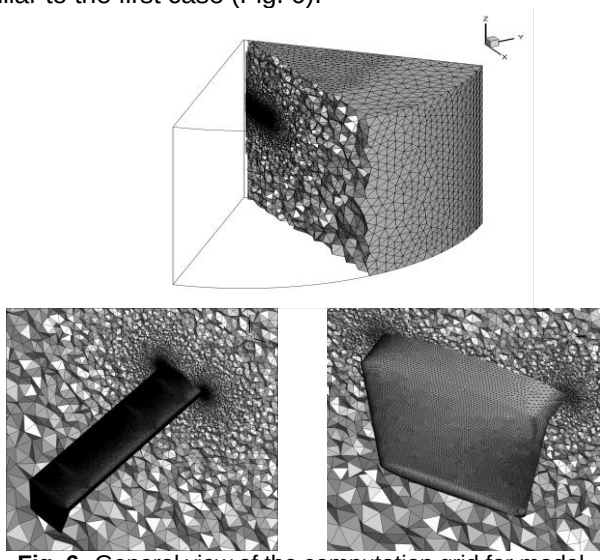

Fig. 6. General view of the computation grid for model main rotor.

Mesh sizes represented in the table below:

Computation grid dimensions for different pitch angles for the model main rotor case

Pitch angle α,deg	Mesh nodes number	Number of elements
5	4145399	24137856
10	4146578	24180511
15	4144917	24134870
20	4144431	24132036

The computation grids were constructed using the ICEM CFD program from the ANSYS software package [10].

5. RESULTS OF THE CALCULATIONS

5.1. General flow pattern

In the calculations a stationary, that is, independent of the angle of rotation ψ, solution was obtained.

In Fig. 7 the flow pattern is presented in the fixed coordinate system for the configuration with the blade pitch angle of 30^o. In plotting this figure the complete flow pattern was obtained by continuing the solution obtained for a single sector with the appropriate rotation of the coordinates of each sector and the velocity vector in the sector by an angle $2\pi k/4$, where

k varied from 0 to 3.

As can be seen in Fig. 7, the streamlines in the flow ahead of the rotor are directed along the axis inside the ring and are gradually curving toward the ring, so that the effect of air suction from the ambient at rest in the channel formed by the ring is observable. The suction velocity diminishes along the ring radius and becomes negligibly small on the outside surface of the shroud. In a flow behind the rotor the axial flow velocity considerably increases on a cylindrical surface of the order of the ring radius and the flow is swirled in the direction of the rotor rotation. With decrease in the radius and increase in the distance the axial velocity diminishes and, as a result, the flow swirling increases. The streamline roll-up into a cord is particularly clearly visible beneath the central body, where the axial velocity is almost zero. This means the formation of helical vortices in the lower flow region, in the vicinity of the axis of rotation.

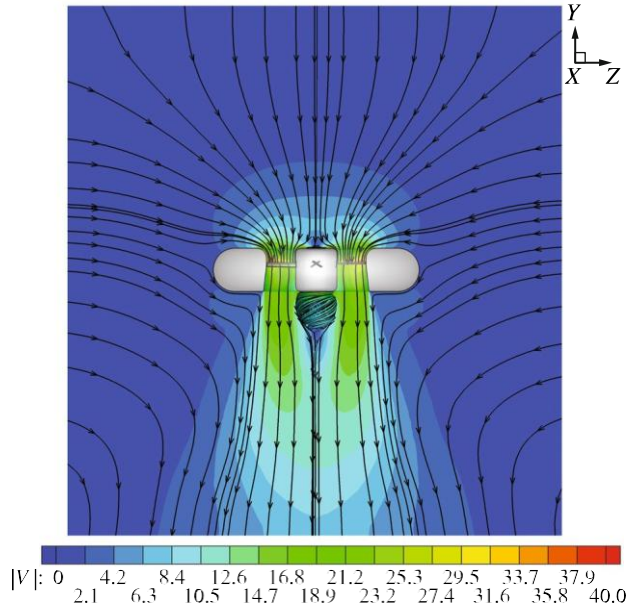

Fig. 7. General view of the flow; streamlines in the fixed coordinate system and the field of the absolute value of the velocity in the meridional section for the blade pitch angle of 30°.

Figure 8 presents the streamlines and the fields of the absolute value of the absolute velocity in the meridional section along the rotor blade axis for different blade pitch angles. Clearly that the greatest flow velocity can be observable in the jet directly beneath the rotor disk, the flow velocity rapidly decreasing with the distance from the ring. An increase in the velocity and the jet width behind the rotor with increase in the blade pitch angle is also observable, although the general flow pattern does not experience considerable variations: a suction zone is formed in the upper half-plane above the ring, a jet outflow zone occurs in the lower half-plane, directly beneath the rotor disk, and the zone of a cocurrent flow induced by the jet flow exists far away from the axis of rotation.

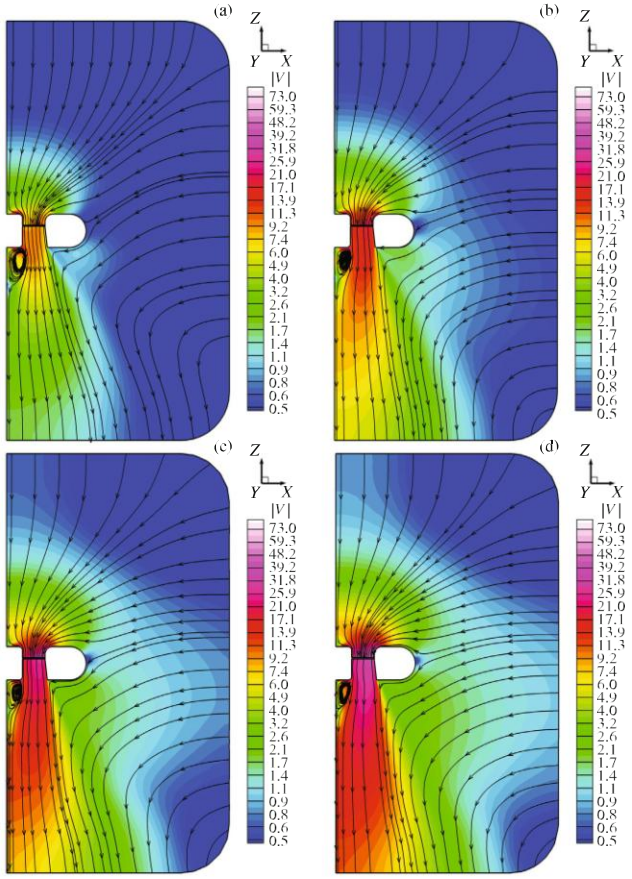

Fig. 8. Streamlines and the field of the absolute value of the absolute velocity in the meridional section for the blade pitch angles of 10°(a), 20°(b), 30°(c), and 40°(d).

5.2. Aerodynamic forces

In Fig. 9 we have plotted the thrust (Fig. 9a) and torque (Fig. 9b) coefficients obtained in the calculations and in the experiment against the blade pitch angle. Obviously, with increase in the pitch angle the axial velocity of the expelled air body behind the rotor increases, while the pressure in the region above the blade reduces. Accordingly, the thrust and the torque coefficient increase. It can be seen that the calculated coefficients are similar in value with the measured ones for all pitch angles for which the calculations were carried out. Good agreement with the experiment is also observable in Fig. 9c in which the rotor polar (thrust coefficient–torque coefficient relation) is plotted. Clearly that the calculated data well fall on the experimental curve.

In the Fig. 10 the model main rotor thrust, torque and polar compared with the experiment measurements.

Like in previous case the calculated results are close to the experiment.

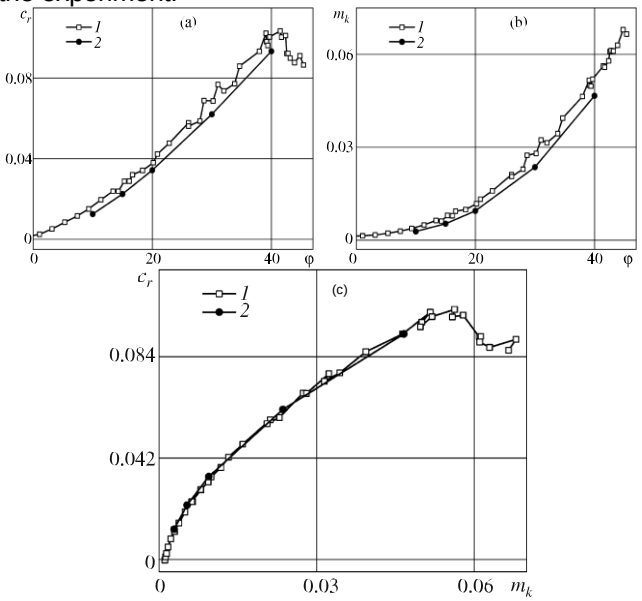

Fig. 9. Shrouded rotor torque (a), thrust (b) coefficients and polar (c); (*1*) experiment and (*2*) calculations.

The calculations on the above-mentioned grids were carried out using the computational structures of the Joint Supercomputer Center of the Russian Academy of Sciences (MVS-10P cluster [11]). The calculations were performed using the NOISEtte software package in the parallel regime using 200 to 480 computational cores with the two-level MPI+OpenMP parallelization [3]. The calculations of one configuration for a fixed blade pitch angle at a fixed rotor rotation velocity took about one day of the computer time.

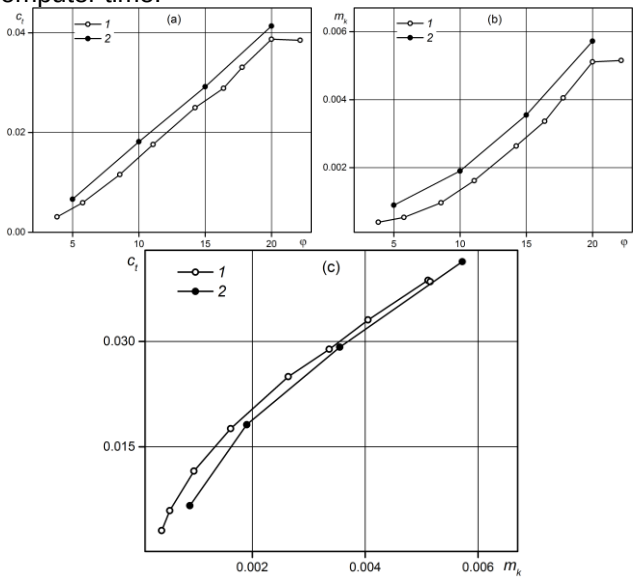

Fig. 10. Model main rotor torque (a), thrust (b) coefficients and polar (c); (*1*) experiment and (*2*) calculations.

6. SUMMARY

Viscous gas flow generated around a model shrouded tail rotor of a helicopter and model main rotor is numerically investigated. The numerical technique developed is validated against the numerical and experimental data on the aerodynamic characteristics of the rotor in the absence of outer flow (hovering operation regime). It is shown that implemented technique applicable for rotors aerodynamic properties prediction.

It should be noted that the computation grids used in this study make it possible to obtain only stationary flow and, accordingly, to use a simplified model of the far field acoustics which accounts for multiple discrete tones of the acoustic field produced by the rotor rotation. At the same time, the broadband eddy noise caused by vortical interactions and small-scale turbulence remains beyond the scope of the study. Later, by means of conducting selective calculations on detailed grids we are planning to investigate the broadband component effect on the acoustic radiation power and its spectral composition in the far field. Supposedly, as applied to the shrouded rotor configuration considered the broadband noise is not particularly noticeable in the far field. However, its adequate modeling is of key importance in numerically investigating the main helicopter rotor and, possibly, actual tail rotor configurations.

REFERENCES

1. I. Abalakin, P. Bakhvalov, and T. Kozubskaya. Edge-Based Reconstruction Schemes for Prediction of Near Field Flow Regions in Complex Aeroacoustics Problems, *Int. J. Aeroacoustics*, 2014, **13** (3-4), 207-233.
2. Ilya Abalakin, Pavel Bakhvalov and Tatiana Kozubskaya. Edge-Based Reconstruction Schemes for Unstructured Tetrahedral Meshes. *Int. J Num. Meth in Fluids*, 2016, **81** (6), 331-356.
3. Abalakin I.V., P.A. Bakhvalov, A.V. Gorobets, A.P. Duben, T.K. Kozubskaya. Parallel research code NOISEtte for large-scale CFD and CAA simulations. *Vychislitelnye Metody i Programmirovanie* (*Numerical methods and Programming*), 2012, **13**, 110-125, (in Russian).
4. W. Johnson, *Helicopter Theory*, Dover Publ., New York, 2013.
5. Ch. Hirsh, *Numerical Computations of Internal and External Flows: The Fundamentals of Computational Fluid Dynamics*, Butterworth-Heinemann, Amsterdam, 2007.
6. H. Pomin and S. Wagner. Navier–Stokes Analysis of Helicopter Rotor Aerodynamics in Hover and Forward Flight. *J. Aircraft*, 2002, **39**(5), 813-821.
7. R. Steijl, G.N. Barakos, and K. Badcock. A Framework for CFD Analysis of Helicopter Rotors in Hover and Forward Flight. *Int. J Num. Meth in Fluids*, 2006, **51**(8), 819-847.
8. P.A. Bakhvalov. Quasi one-dimensional reconstruction scheme on convex polygonal meshes for solving aeroacoustics problems. *Mathematical Models and Computer Simulations*, 2014 **6** (2), 192-202.
9. Y. Saad, *Iterative Methods for Sparse Linear Systems*, Soc. Industr. Appl. Math., Philadelphia (2003).
10. ANSYS ICEM CFD. http://www.cae-expert.ru/product/ansys-icem-cfd
11. Joint Supercomputer Center of the Russian Academy of Sciences. http://www.jscc.ru